

Chapter 6

Induction Cell Design Tradeoffs and Examples

Louis L. Reginato and Richard J. Briggs

6.1 Introduction

A brief history of induction accelerator development was covered in [Chap. 2](#). The induction accelerators constructed since the early 1960s can be categorized as short-pulse if the pulse duration is less than 100 ns and long-pulse if it is longer. The distinction between short-pulse and long-pulse is arbitrary; it mainly reflects the type of magnetic material that was typically used in the cell. Examples of short-pulse induction accelerators are the electron ring accelerator (ERA, $\Delta t = 30$ ns) [1], the advanced test accelerator (ATA, $\Delta t = 70$ ns) [2] and the experimental test accelerator (ETA-II, $\Delta t = 70$ ns) [3]. Examples of long-pulse accelerators are the Astron ($\Delta t = 400$ ns) [4, 5] and the second axis of the dual axis radiographic hydro test accelerator (DARHT-II, $\Delta t = 2,000$ ns) [6]. In this chapter the cell design of several of these accelerators will be described in detail. We will discuss how the physics, economics, and space requirements often lead to a non-optimum design from the accelerator systems vantage point. Although modulators are covered in [Chap. 4](#), some specific designs will be discussed on how the constant voltage (flat-top) was achieved in concert with the cell design and compensation network.

6.2 Cell Configurations

Induction cell designs for the short and long-pulse accelerators are as varied as the applications for which they were intended. The long-pulse cell cross-section of the Astron and the DARHT-II accelerators are contrasted in [Fig. 6.1](#). The short-pulse cell cross-section of the ATA and the ETA-II accelerators are shown in [Fig. 6.2](#).

A comparative analysis of each design reveals important features distinctive to each cell. The constraints imposed by the physics requirements often limited the optimization process to achieve the best performance and efficiency at a minimum cost.

L.L. Reginato (✉)
Lawrence Berkeley National Laboratory, Berkeley, CA 94720-8201, USA
e-mail: LLReginato@lbl.gov

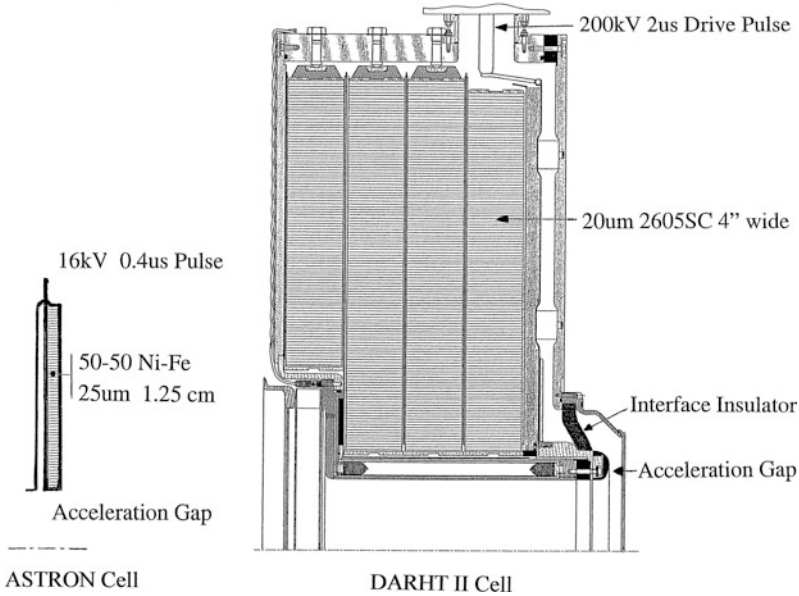


Fig. 6.1 Cell cross-section of the Astron and DARHT-II accelerators

It has been customary to show the induction cell as a one-to-one coupled transformer, but it may actually be represented more accurately as an auto-transformer. The simplified equivalent circuit discussed in [Chap. 3](#) is repeated here in [Fig. 6.3](#) for continuity. V_S and Z_S are the voltage and impedance of the pulse generator, Z_L is the compensation load, L_c is the inductance of the cell, I_c represents the core magnetizing current which includes losses, C_g is the acceleration gap capacitance, I_B is the beam load and V_c is the acceleration voltage. It is evident that the beam current is supplied directly from the pulse generator and that the sole function of the magnetic core in the cell is to provide a high impedance to ground for the full duration of the pulse. As discussed in [Sect. 3.5](#), the core volt-seconds product $V_c \Delta t = A_c \Delta B$ must be sufficient so that the magnetic material does not go into saturation during the pulse. Here, A_c is the core cross-sectional area, Δt is the pulse duration and ΔB is the flux swing averaged over the core cross section.

Turner presents comparative measurements of the ETA-II and the ATA core impedances [7]. The ETA-II cell design by Birx shown in [Fig. 6.2](#) shows considerably less impedance variation than the ATA. The ETA-II cell configuration closely resembles a ferrite loaded transmission line while the ATA is driven from the outside diameter and behaves more as a lumped element with more impedance variation. Another design improvement on the ETA-II cell is that the ferrite cores, just behind the interface ceramic insulator, were closely coupled to the BBU RF modes and provided the necessary damping without additional ferrites. Despite the lower impedance variation of the ETA-II cell, a compensation network was still required to maintain a constant voltage because the magnetizing current (sometimes

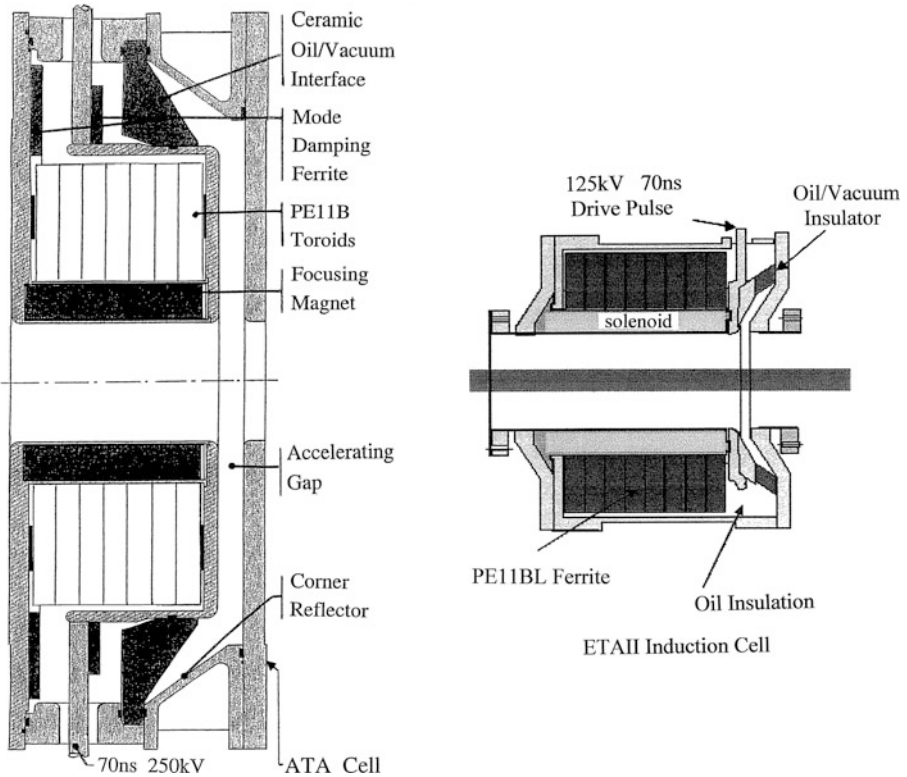


Fig. 6.2 Cell cross-section of the ATA and the ETA-II accelerators

called leakage current) was a much larger fraction of the total current than was the case in the ATA drive system.

From the simplified equivalent circuit in Fig. 6.3, it can be seen that with a constant V_s , the time-varying current required for core magnetization flowing through Z_s will cause a time-varying acceleration voltage, V_c . This is not acceptable since most experimental programs require a constant voltage during the pulse flat-top.

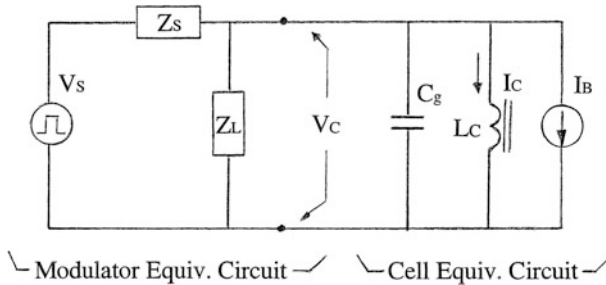


Fig. 6.3 Simplified equivalent circuit of induction unit

There are several techniques or combinations thereof that can be used to insure that the acceleration voltage, V_c , remains constant. They are:

- (a) Make the core magnetizing current, I_c , much smaller than the total current from the source.
- (b) Introduce an impedance, Z_L , in shunt with the cell impedance which complements it in such a way as to make the combination approximate a constant load on the source.
- (c) Design the source impedance, Z_s , so that it varies in time and supplies the current required by the core.
- (d) Make the source impedance much smaller than the core impedance.

In describing the simplified equivalent circuit, Z_s has represented the source impedance of the pulse generator or modulator. In most cases, induction cells are driven by long cables from a modulator located a distance away. Typically, the cable length is chosen so that the two way travel time is equal to or greater than the pulse duration τ_p . That is, the cable length $\ell > (\tau_p/2)v$ where v is the wave speed in the cable. This is done to avoid cell-to-cell interaction when they are driven from the same modulator. It also eliminates reflections from beam head induced transients from reflecting back during the pulse and locates the modulator in a radiation free environment for easy maintenance. In this case, Z_s , actually represents the cable impedance and not the source impedance of the modulator. In most accelerators, the cable impedance is matched to that of the modulators so it is also correct to say that Z_s represents the source impedance.

It is apparent from the simplified equivalent circuit that the voltage on the cell will droop with an exponential decay time determined by the L_c/Z_{eq} , where L_c is the inductance of the cell and Z_{eq} is the parallel combination of Z_s and Z_L . The inductance is dependent on the aspect ratio of the cell but mostly on the properties of the magnetic material. With square loop materials, the droop can be fairly simple to compensate but with materials with a complex $B-H$ relationship it can be a difficult task. As discussed in Sect. 6.4, the pulse flat-top on the ATA was achieved by choosing method (a) listed above. That is, the ferrite magnetizing current was made sufficiently small that the droop was less than 1%, thus requiring no compensation. In the Astron accelerator, method (b) was used by installing the pulse-shaper circuit to maintain the flat top over the 400 ns pulse. Note that in this case the beam was a small fraction of the total current and because of the highly nonlinear L_c , the compensation network was quite complex and used most of the energy. In the DARHT-II accelerator with cable length a small fraction of the total pulse duration, method (c) was used. In this case, the pulse forming network characteristic impedance was tapered to make the equivalent modulator source impedance, Z_s , time-varying to compensate for the magnetic material nonlinearities. With the development of solid state modulators (see Chap. 4), method (d) offers a viable solution to maintaining the flat-top during the pulse. The energy in an on/off solid state modulator comes from a large capacitor where the source pulse impedance is essentially zero except for some small stray series inductance. In this case, the modulator can supply any

amount of current and still maintain a flat-top as long as it is in close proximity of the cell. If long cables are used to power the cell, then the issue becomes more complex and compensation may be required.

6.3 Long-Pulse Cell Design

For optimum efficiency and best performance it is always advantageous to minimize the magnetizing current. It is important to choose a magnetic material with high permeability and a cell aspect ratio (outer to inner radius) which leads to high inductance. The high gradient required by the Astron accelerator led to a cell design with very short axial length and large ratio of outer to inner radius as shown in Fig. 6.1. This design resulted in a small and very nonlinear cell inductance since the inductance is proportional to the length of the cell and to the log ratio of outer to inner radius. The large nonlinear load current was further aggravated by saturation at the inner core radius. The Astron drive system is shown in Fig. 6.4. The modulator was implemented by using six parallel cables to form a pulse forming line (PFL) switched by a thyatron. The six cables had a linear source impedance of 8.33Ω and the nonlinear magnetizing current was compensated by the three harmonics “pulse-shaper” to produce a constant acceleration voltage. The PFL delivered a total of 2 kA into a matched load with 400 A going to the beam and 1,600 A to the magnetizing current and pulse-shaper. It is interesting to compare this design to one with lower gradient had it been allowed by the physics design. For example, maintaining the same core cross-sectional area, if the cell had been made 5 cm long axially, it would have resulted in 48% greater inductance and a core volume reduction of 60% leading to a simpler pulse shaper and considerably lower modulator energy and cost. This observation does not suggest that the physics design or requirements should be compromised but simply points to the importance of carefully studying the tradeoffs between the physics design and the engineering implementation since they can have a significant impact on the system performance and cost.

The DARHT-II induction cell shown in Fig. 6.1 also required a large aspect ratio in order to satisfy the pulse duration and energy gain while fitting within a pre-existing building. The initial beam current required was 2 kA with allowance for future expansion to 4 kA. Once the beam transport physics determined the inside

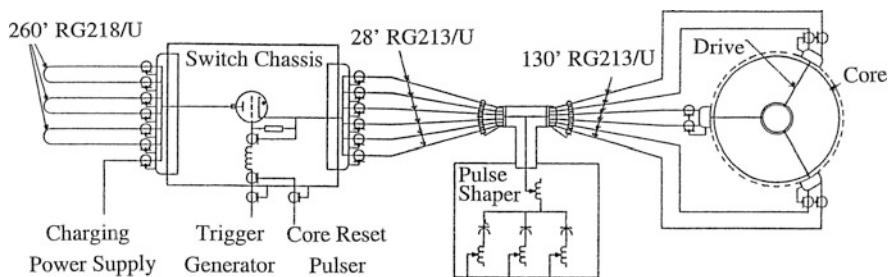


Fig. 6.4 Astron accelerator drive system

radius to achieve transverse stability, as discussed in Sect. 6.10, the cell geometry was pretty well established. All that remained to be done was to choose the highest ΔB material that fit within the economic boundary dictated by the project. A number of materials from several manufacturers were considered and tested. Budgetary constraints quickly eliminated all of them except the as-cast 2605SC Metglas produced by Allied Signal Corporation. In order to stay within the allotted budget, the 20 μm material had to be cast in widths of 10 cm or wider. The hysteresis loop for a full size core for the DARHT-II accelerator is shown in Fig. 5.4 and it shows that the nonlinear portion of the magnetizing field will have a peak value of ~ 500 A/m which translates to 1.6 kA of peak current for the DARHT-II cell. It was decided that in order to meet all the programmatic requirements, a total current drive of 10 kA would be chosen. Since the nonlinear portion of the current was about 16% of the total, the constant voltage requirement was met by designing a pulse forming network (PFN) with temporally decreasing impedance which matched the nonlinear (time-varying) impedance of the core. The PFN chosen was a modified type-E network with an average impedance of 20 Ω and a 2 μs output pulse of 200 kV into a matched load. The capacitors were chosen to have the same value and in order to achieve the decreasing impedance, the inductors were reduced in value from the front to the back of the pulse (PFN). Figure 6.5 shows the acceleration voltage waveform for the DARHT-II cell at 20% below operating level. The amplified waveform shows that a $\pm 1\%$ variation could be achieved by careful tuning of the PFN stage inductance.

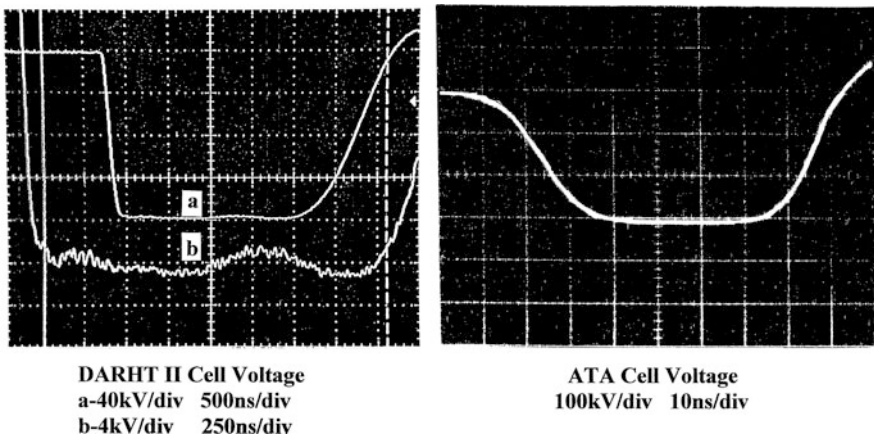


Fig. 6.5 DARHT-II and ATA cell voltages

6.4 Short-Pulse Cell Design

The cross-section of the ATA and ETA-II induction cells are shown in Fig. 6.2. The ETA-II cell was an improved design that could operate at high repetition rates with one half the gradient and one tenth the current of the ATA. Since the ATA cell was

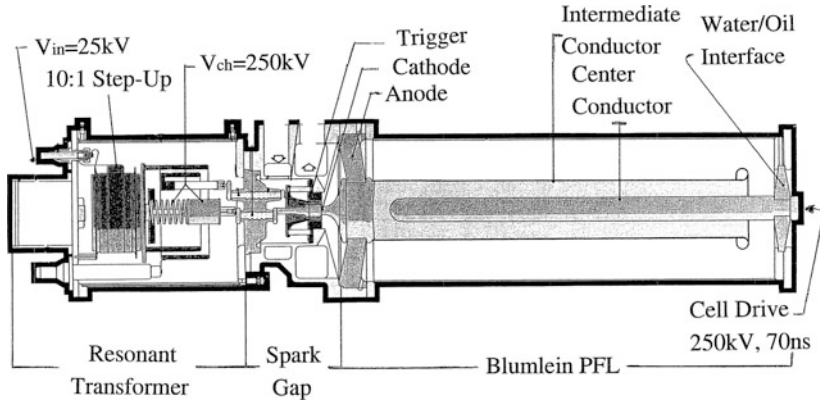


Fig. 6.6 ATA 250 kV, 70 ns pulse generator

the more challenging design, it will be discussed in more detail. Each of the 200 ATA cells were designed to deliver a 70 ns, 250 kV pulse at 20 kA for a total of 50 MeV. The modulator is shown in Fig. 6.6. It consists of a 12.5Ω Blumlein PFL charged by a double resonant transformer and switched by a gas-blown spark gap. The pulse is delivered to the cell symmetrically by two 25Ω oil filled cables. The cell was considered to be very nearly an optimum design in that it delivered the desired gradient and energy uniformity with high efficiency without a compensation network. The core material was TDK's PE11B Ni-Zn ferrite which required only ~ 500 A of magnetizing current to achieve full flux swing from $-B_r$ to $+B_s$. The equivalent series impedance of 12.5Ω resulted in a voltage droop of about $\pm 1\%$ during the 70 ns pulse. The beam transport system allowed for this variation and no compensation network was needed to improve it. Except for the heavy ion fusion program, efficiency is usually not a high priority in induction accelerators. However, it is interesting to note that had the ATA accelerator been able to transport a 20 kA beam, the cell efficiency in energy delivery would have been 97%. The voltage waveform is shown in Fig. 6.5 and because the cell is being driven 25% above the operating level, core saturation shortens the pulse and the voltage flat-top.

6.5 Comparison Between Amorphous and Ferrite Cells

The previous examples have shown how the induction cell design for previous long- and short-pulse accelerators were implemented using unique engineering designs in order to satisfy the physics requirements. A number of tradeoffs were required which in some cases led to non optimum designs from the standpoint of pulse waveform compensation and efficiency. It was shown that if a high gradient is required, large diameter and short axial length cores lead to a highly nonlinear (time-varying) current drive which makes the compensation for constant voltage during the pulse considerably more difficult.

As previously mentioned, the cross-over point between short-pulse and long-pulse was arbitrarily selected at 100 ns. It was pointed out that ferrites are more applicable to the short pulse while the ferromagnetic materials are preferred for the long pulse. However, the ferromagnetic materials, in particular the amorphous and nanocrystalline ones, have also been used in short-pulse applications such as nonlinear pulse compression modulators as well as induction cells. Their use has not been confined exclusively to long pulses so their application depends on many factors.

The following example will show that 100 ns is a reasonable cross over point between the usage of ferrites and amorphous materials in induction cells. Design parameters for two cells are presented for the following parameters:

Accel. Voltage	100 kV
Pulse Duration	100 ns
Axial Length	0.1 m
Inside Radius	0.1 m

One design employs the PE11B Ni-Zn ferrite used in the ATA and the other is based on the 2605SC as-cast amorphous material used in DARHT-II. The voltage gradient will be the same as will be the inside radius and the pulse duration. Two comparisons are made. In Case I the maximum flux swing for each material will be used and in Case II the cross-sectional area (including packing-factor) of the amorphous material is made the same as that of the ferrite. The results are shown in Table 6.1. The packing factor which is the ratio of the cross-sectional area occupied by the magnetic material to the total cross sectional area is assumed to be 0.75 for 2605SC and 1.0 for PE11B. The losses are obtained from Fig. 5.5 by applying the respective magnetization rates (dB/dr) for the two cases. In Case I where the maximum flux swing applicable to each material is utilized, the losses for PE11B are 2.3 J and for 2605SC the losses are 23.7 J. In Case II, where the same cross sectional area is used resulting in a lower magnetization rate for the 2605SC material, the losses actually increase. This result is somewhat surprising and can be explained by the fact that at the lower magnetization rates, the total losses for the amorphous material 2505SC increase because the decrease in losses per unit volume are offset

Table 6.1 Comparison of losses between PE11B Ni-Zn Ferrite and the 2605SC as-cast amorphous material used in the DARHT-II induction cells

Quantity	Ferrite	Metglas 2605SC	
	PE11B	Case I	Case II
Flux swing [T]	0.6	2.4	0.8
Coercive force [kA/m]	0.2	2.9	2.5
Outer radius [m]	0.267	0.156	0.267
Magnetization rate [T/ μ s]	6	24	8
Energy loss [J]	2.3	23.7	28.8
Volume [m ³]	0.0193	0.0045	0.0145

by the proportionally greater increase in total volume. The large increase in total volume also explains the fact that that average coercive force is nearly the same in the two cases. In either case, the amorphous material is not competitive with the Ni–Zn ferrite in terms of losses. For low current accelerators using 2605SS, the magnetizing current would be excessively large and the modulator peak power would have to be ten times greater than that for the ferrite.

There are other factors that should also be taken into consideration. For example, the choice of material also depends on the total beam current that must be accelerated, the nonlinearity of the respective $B-H$ loops, modulator cost and the cost and quantity of magnetic material that is needed. If the beam load is much larger than the magnetization losses, the core losses will not be the major deciding factor in choosing the material. Other important factors to be considered before making a final choice include repetition rate, high voltage integrity of the cell and the influence of the core material on the damping of the beam break-up instabilities. Ferrites with very high resistivity are basically an insulator and high voltage integrity is much easier to achieve than with amorphous materials. The other very important factor to consider is the attenuation of the high frequency modes that cause beam instability. Accelerator cells that use amorphous materials must have ferrites near the acceleration gap to attenuate the BBU modes. In cells that use PE11B or PE11BL, such as the ETA-II in Fig. 6.2, if the ferrite is exposed to the acceleration gap the additional BBU absorbers are not required.

The accelerator designer needs to take into consideration all the issues that were mentioned in making the final decision on whether to use ferrites, amorphous or nanocrystalline materials at any pulse duration. However, the use of ferrite at pulse durations of 100 ns or less appears to offer several distinct advantages. If the core dimensions are such that the ferrites cannot be manufactured as a toroid or very high gradients are required, then the only choice may well be to use an amorphous or nanocrystalline material.

6.6 Core Segmentation and Flux Equalizing

The conventional low gradient three-cell configuration giving a voltage gain $3V$ is shown in Fig. 6.7a. To achieve a three times higher gradient and still maintain a linear drive and avoid core saturation, two techniques have been used as shown in Fig. 6.7b, c. One such technique called core-segmentation has been used in the injector at the National Bureau of Standards in the 1970s, the relativistic two-beam accelerator (RTA) in the late 1990s, and the prototype cells of the Heavy Ion Fusion Accelerator [8–11]. It can be seen from Fig. 6.7c that in cases where large ratios of outside to inside diameters are unavoidable, the core can be split radially in several sections resulting in lower core saturation on the inside diameter thus reducing the non-linearity of the magnetizing current. The high voltage feed must encircle each core individually and is V in value. If as shown in Fig 6.7c there are three segments, the total voltage gain is $3V$ and the total current consisting of beam plus magnetizing current will be slightly greater than that of the drive for the three

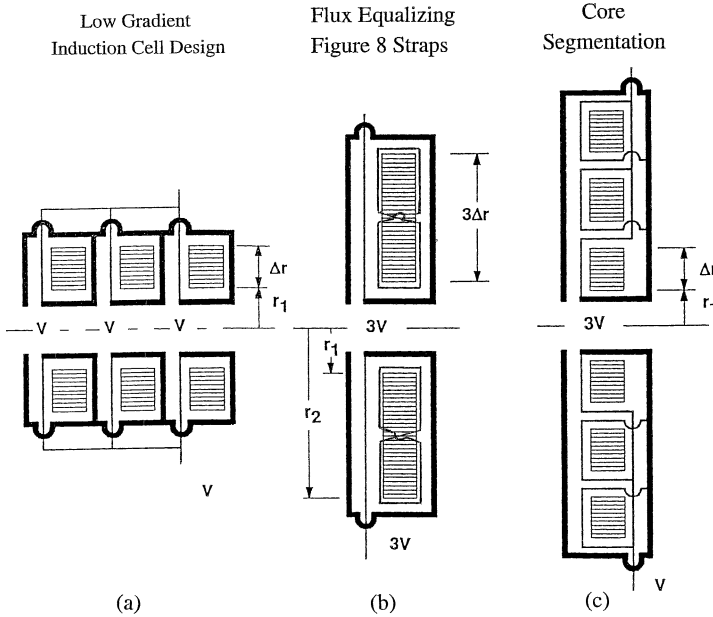


Fig. 6.7 Conventional low-gradient, three-series cells (a), higher-gradient, single-cell with figure eight strapping (b), and higher-gradient cell with core segmentation (c)

low gradient cells. In order to maintain the required high voltage safety factors in the drive conductors, radial and axial space must be added to the cell design. The loss of radial and axial packing factor, the increased complexity of the high voltage feeds and a lower impedance reduce the effectiveness of core-segmentation. It does not necessarily lead to a better or more desirable overall system configuration. To satisfy the high gradient requirements, the cell designer must consider the advantages of core segmentation against the disadvantages of increased complexity in the network compensation to achieve linearity of drive and constant voltage. Since core-segmentation has mainly been used in injectors, the beam break-up cell impedance issues have not been addressed for this configuration.

Another technique which has been suggested to equalize the flux density from the inside to the outside radius of the core is to couple the flux from the inside half to the outside half by a figure eight conductor as shown in Fig. 6.7b. Since the magnetization rate is greater on the inside portion, the figure eight conductor couples the flux to the outside half forcing them to be equal. The voltage drive in this configuration is $3V$ and the current will be about one third that of the three-core drive leading to a nine times higher impedance. Similarly to the core segmentation case, to insure high voltage integrity of the figure eight conductors, the packing factor is also decreased axially and radially reducing the effectiveness of this technique. In actual prototype tests, flux equalizing between the inside and outside halves of the core were only partially effective. This lack of agreement with the expected results can partly be

attributed to the leakage coupling between the inside to the outside loops and may be made more effective by additional figure eight radial straps.

The need to apply core segmentation or flux equalizing in high gradient cells where the ratio of outside to inside diameter is large in order to reduce impedance nonlinearities must be decided on an individual basis. One needs to insure that the benefits outweigh the increased complexity of the compensation network [12–14].

6.7 Core Reset Techniques

In all short- and long-pulse accelerators in order to make full usage of the flux swing, the magnetic core in the cell must be reset from the remanent flux $+B_r$ back to $-B_r$ or $-B_s$ after the forward or main acceleration pulse. The reset is usually accomplished by applying a pulse of opposite polarity to the core through an isolation inductor such as in the Astron and DARHT-II accelerators. The core reset can also be accomplished by directing the PFL charging current through the core in the opposite direction of the forward pulse as was done in the ATA accelerator avoiding the need for a separate pulse generator. As discussed in Sect. 5.4, the reset pulses are typically of much longer duration and much lower energy than the main pulse, but sufficient to provide enough current to bias the core near $-B_s$.

In high gradient cases where it is critical to achieve the absolutely maximum flux swing, it is possible to gain additional ΔB from $-B_r$ to near $-B_s$ by maintaining the reset current flowing through the core during the main pulse as was done in the ATA and DARHT-II. This technique is particularly beneficial in magnetic materials with low remanence such as the as-cast 2605SC or some Ni–Zn ferrites.

In the ATA, the Blumlein charging current flows in the reverse direction through the cell resetting the core to $-B_r$. If the spark gap is triggered just prior to the peak resonant voltage, the current maintains the core near $-B_s$ rather than $-B_r$. In the DARHT-II cell, the reset is accomplished by a separate pulser and the reset current is likewise kept flowing prior to the forward pulse beginning the cycle near $-B_s$ gaining additional ΔB . A considerable amount of magnetic material can be saved using “active reset” at the expense of a slightly more complex compensation network to maintain constant voltage. The active reset may also be used as a tuning knob to make small adjustments on the operating range of the hysteresis curve.

6.8 High Voltage Design Issues

The magnetic material (core), the high voltage cable feeds and the compensation network are typically immersed in oil. The beam undergoing acceleration and focusing in the accelerator is in high vacuum. The interface separating these two regions is a critical component of the cell (see Figs. 6.1 and 6.2). This insulator must reliably hold off the acceleration voltage without arcing and it must resist shocks and not deteriorate if arcing does occur. This insulator is typically hidden from the beam

line of sight since it is believed that stray particles landing on the insulator lead to surface breakdowns. As discussed in Sect. 6.10, another very important function of this insulator is to allow the transmission of the beam break-up modes into the ferrite dampers located just behind it on the oil side so the high frequency properties are also very important. The choice and the angle of this insulator must follow established high voltage practices covered extensively in the literature.

To satisfy the vacuum requirements in the ETA-II and the ATA, the interface insulators were made of ceramic and the DARHT-II used Mycalex. Figure 6.1 and 6.2 show the interface insulators for the long- and short-pulse induction cells which satisfy both the equipotential angle requirement for optimum voltage holding and BBU mode transmission to the ferrite dampers. As discussed in Sect. 6.10, the acceleration gap spacing directly impacts the growth of the beam instabilities. That is, the narrower the acceleration gap, the lower will be the growth. This is in direct conflict with the voltage holding requirements which demand a wide gap for reliable operation. At the desired beam current, a balance must be achieved which satisfies both the beam transport stability and the high voltage requirements with acceptable risk factors.

In the last decade, a new type of insulator has been developed which has achieved voltage gradients several times greater than the conventional angled insulator. It is less sensitive to bipolar voltage pulses, is not susceptible to the presence of high current beams and also satisfies the BBU transmission requirements [15]. This insulator is based on a well known fact that the more grading that is applied to a vacuum surface, the greater will be the voltage that it can hold without arcing. The high gradient insulator concept takes the grading to extremes by alternating layers of conductors and insulators with a period of about one millimeter. The properties of this insulator have been well established and the only drawback appears in the manufacturing of different shapes and sizes. In recent times, however, techniques for manufacturing this insulator in large quantities at reasonable cost have made great strides and it will undoubtedly be used in future induction cells [16].

Another very important issue in the cell design is the voltage distribution between the cores and the cell. In short pulse accelerators where Ni-Zn ferrite with high resistivity is used, the voltage distribution is relatively uniform and it is not an issue. In long-pulse cells with many individual cores of amorphous material such as the DARHT-II cell shown in Fig. 6.1, the voltage distribution must be carefully analyzed since statically these cores act like a short and dynamically they act as voltage generators dependent on the radial distribution of the flux density in the core. It is evident that the voltage induced by each core will be proportional to the cross sectional area and in this case will be approximately one fourth of the total voltage. Also intuitively one can estimate that if the core-to-core and the core-to-end plate spacing is identical and the capacitance from the outside diameter of the cores to the inside diameter of the vessel is negligibly small, equal voltages should appear core-to-core and core-to-end plates. As discussed in Sect. 6.9, however, because of radial core saturation effects, unequal core-to-core and core-to-end plates capacitance and non negligible core-to-inside vessel capacitance, the voltage will not be equally distributed. Accurate analysis of the voltage distribution is essential to determine

the proper high voltage insulation from core-to-core and core-to-end plates to insure that safe operating voltage gradients are maintained.

To insure that there are no high voltage breakdowns, the cell is typically filled with insulating oil. Critical to reliable voltage holding is the removal of all air from the cell prior to filling with out-gassed oil. Furthermore, in cores that are wound with as-cast amorphous alloys with inter-laminar insulation, the ribbon must be carefully wound so that individual layers do not protrude or shift after winding to create razor edges with excessively high gradients which might lead to voltage breakdown.

6.9 Voltage and Electrical Stress Distribution in Laminated Cores

In this section we analyze the electrical stress distribution in laminated cores like the DARHT-II cell shown in Fig. 6.1. In the long-pulse regime where laminated cores are used, a quasi-static approximation for the electromagnetic fields generally suffices because the timescale for the fields to change is much longer than the EM wave propagation time. Applying this approximation has subtle features because the electric field is a mixture of an “inductive emf field” (having a nonzero curl, with \dot{B} the source) and a “quasi-electrostatic field” (the source being electric charges on the various metal surfaces).

“Micro-scale” core fields: We first discuss the EM field structure on the “micro-scale” of the individual layers of magnetic ribbon (for example, Metglas) and the insulation between them (for example, Mylar). Inside the Metglas the radial electric field (normal to the interface) is negligible. It is shorted out by the high Metglas conductivity ($1/\sigma \approx 1.25 \times 10^{-6} \Omega\text{m}$) on the timescale ϵ/σ for surface charges to build up on the interface.

The magnetizing current flowing around the entire core creates an $H_\theta \sim 1/r$ field that is constant throughout an individual Mylar sheet. To illustrate the main features of the “micro-scale” EM fields, we first analyze the simplest case where the effective “skin depth” is much larger than the Metglas thickness d_M , and take both H_θ and $B_\theta = B_M$ as constant throughout the Metglas tape as well. (This approximation is valid in DARHT-II, for example [17]). Inside the Metglas (see Fig. 6.8) Maxwell’s equations require

$$\left(\frac{\partial E_z}{\partial r} \right)_M = \frac{\partial B_M}{\partial t}. \quad (6.1)$$

The net current in the z direction in any Metglas tape section must be zero, otherwise free charge at the ends of the tape would rapidly build up. The axial electric field inside a given Metglas layer must therefore be an odd function of $r - r_n$, where r_n is the center of the n th Metglas layer;

$$E_z = (r - r_n) \frac{\partial B_M}{\partial t}. \quad (6.2)$$

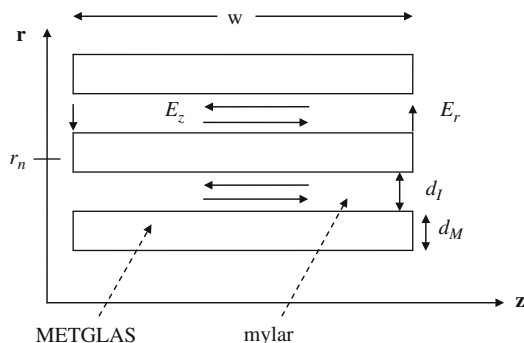


Fig. 6.8 Expanded view of Metglas and Mylar ribbon tape

Since this solution is essentially the same in adjacent tapes (H_θ varies slowly on this scale), the E_z field must vary in the periodic fashion indicated in Fig. 6.8 from tape to tape. Therefore the slope of $E_z(r)$ in the Mylar region must be $-d_M/d_I$ times the slope of $E_z(r)$ in the Metglas region given by Eq. (6.1).

In the case treated here where the skin depth is larger than the ribbon thickness, the eddy current flowing in the axial direction in the ribbon (σE_z) varies linearly in r across the ribbon. Integrating the power dissipation in the ribbon (σE_z^2) across its thickness using Eq. (6.2), we see that the average power per unit volume dissipated in the core from the resistive losses is proportional to

$$P_d \sim \sigma \left(\frac{dB}{dt} \right)^2 d_M^2. \tag{6.3}$$

The energy loss associated with the eddy currents is the dominant loss mechanism in a laminated core at high magnetization rates, as discussed in Sect. 5.4. From Eq. (6.3) we see that the energy loss magnetizing the core through one cycle is proportional to the square of the ribbon thickness, the Metglas conductivity, and the rate of magnetization [see Eq. (5.2)].

In the Mylar where B is very small in comparison to B in the Metglas, $\nabla \times E$ is approximately zero, so

$$\left(\frac{\partial E_r}{\partial z} \right)_I = \left(\frac{\partial E_z}{\partial r} \right)_I = -\frac{d_M}{d_I} \frac{\partial B_M}{\partial t}, \tag{6.4}$$

where $(E_r)_I$ is the radial electric field in the Mylar (normal to the interface).

Outside of the core region, the “smooth” radial electric field in gaps between cores, or between the core and an end plate, should be set equal to the mean value of the radial field (averaged over the layers of Metglas and Mylar tape) at the core boundary:

$$\langle E_r \rangle = \frac{(E_r)_I d_I}{d_M + d_I}. \quad (6.5)$$

Using Eq. (6.4), we have

$$\frac{\partial \langle E_r \rangle}{\partial z} = -\frac{d_M}{d_M + d_I} \frac{\partial B_M}{\partial t} = -p_f \frac{\partial B_M}{\partial t}, \quad (6.6)$$

with the last equality defining the “packing factor” p_f . Since the magnetic field in any individual Metglas tape winding is constant in z , $\langle E_r \rangle$ varies linearly in z across the tape width w .

In cases where the effective “skin depth” is not much larger than the Metglas thickness, the magnetic field B_M will have significant radial variation within each individual Metglas ribbon (as a “saturation wave” propagating inward, for example). In these more general cases, it is easy to show that Eq. (6.6) is still valid as long as we use a radial average over the ribbon of the magnetic field B_M on the right hand side.

In moving over to a “macro” description of the EM fields, note that the maximum value of E_z is of order $d_M/w \sim 10^{-3} - 10^{-4}$ compared to the peak value of $\langle E_r \rangle$. We can therefore safely ignore the z -directed electric field in a “macro-picture,” even though it is a critical factor in the “micro-picture” of the fields in the Metglas that create the eddy currents and associated losses.

Also note that in a macro description, the equivalent radial dielectric constant for calculating the radial displacement current using the mean radial electric field [see Eq. (6.5)] is

$$\epsilon_r = \frac{\epsilon_I}{1 - p_f}, \quad (6.7)$$

where ϵ_I is the Mylar dielectric constant.

We have implicitly modeled the tape sections as individually-nested cylinders instead of the actual continuous helical winding of (typically) thousands of layers. This approximation is valid as long as the radial displacement current is much larger than the real current in the helical windings, which it should be considering the resistance and inductance impeding the real current flow.

Modeling a core as an equivalent homogeneous media: The previous discussion of the “micro-fields” motivates the following description of the “spatially averaged” EM fields (macro-fields) in a core region. These are the fields that will be matched onto the EM fields in gap regions, for example.

The magnetic fields in the core region are basically magnetostatic in character because the large inductance constrains the rate of rise of the magnetizing current I_M , so $H_\theta = I_M(t)/(2\pi r)$. In our formulation we assume that the macroscopic (mean) azimuthal magnetic field $B_\theta(r, t) = p_f B_M$ in any one core is a function of r and t only. Otherwise, one is free to use arbitrary models of the nonlinear magnetization including eddy currents, saturation, etc., as inputs. Since in an equivalent

homogeneous core model, $E_z = E_\theta = 0$, Maxwell's equations reduce to [see Eq. (6.6)]

$$\frac{\partial E_r}{\partial z} = -\frac{\partial B_\theta(r, t)}{\partial t}, \quad (6.8)$$

with the simple solution

$$E_r(r, z, t) = -z \frac{\partial B_\theta}{\partial t} + E_r^c(r, t), \quad (6.9)$$

where E_r^c is independent of z , but otherwise an arbitrary function of r and t at this point. We take $z = 0$ as the center of the core.

For the purpose of matching onto the gap fields, we define ‘‘voltages’’ along the left and right side of the core as

$$\begin{aligned} \psi_L(r, t) &\equiv -\int_a^r dr' E_r(r', z = -w/2), \\ \psi_R(r, t) &\equiv -\int_a^r dr' E_r(r', z = +w/2), \end{aligned} \quad (6.10)$$

where a is the inner radius of the core. We introduce the following definitions of the ‘‘inductive’’ and ‘‘electrostatic’’ voltage components, respectively

$$\begin{aligned} V &\equiv -w \int_a^r dr' \frac{\partial B_\theta(r', t)}{\partial t}, \\ \Phi &\equiv -\int_a^r dr' E_r^c(r', t). \end{aligned} \quad (6.11)$$

Then

$$\begin{aligned} \Psi_L &= \Phi + V/2, \\ \Psi_R &= \Phi - V/2. \end{aligned} \quad (6.12)$$

The inductive voltage $V(r, t)$ is assumed to be known from the magnetostatic modeling of the core. The sources for Φ , as we will see, are the free charges which redistribute themselves on each Metglas layer to short out the internal E_z and E_θ . A differential equation for Φ can be obtained by applying the constraint of no radial conductivity. Consider the ‘‘pillbox’’ shown in Fig. 6.9 encompassing a radial slice Δr that extends over the full width of the core. (Note that this radial slice contains many individual layers of ribbon, since we are treating the core as an equivalent homogeneous media in making a connection with the smooth fields outside the core.) The net displacement current out of the pillbox must vanish, since no charge can flow out of it radially, so

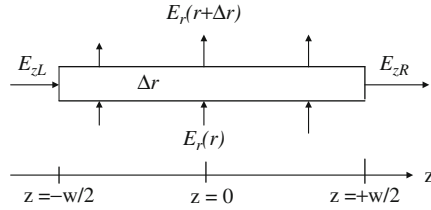


Fig. 6.9 Pillbox used to apply constraint of no net charge flow out of each Δr layer of the core

$$2\pi r \Delta r \epsilon_g (E_{zR} - E_{zL}) + 2\pi \epsilon_r \int_{-w/2}^{+w/2} dz [(r + \Delta r) E_r(r + \Delta r) - r E_r(r)] = 0. \tag{6.13}$$

Here E_{zR} and E_{zL} are the axial electric field components just outside the core at the right and left sides of the core, respectively, ϵ_r is the effective radial dielectric constant given in Eq. (6.7), and ϵ_g is the dielectric constant of the insulating media in the gap region between the core and end plates, or between adjacent cores.

Using the solution for E_r from Eq. (6.9) and the voltage definitions, and taking the limit $\Delta r \rightarrow 0$, we have

$$E_{zR} - E_{zL} = \frac{\epsilon_r w}{\epsilon_g} \frac{1}{r} \frac{\partial}{\partial r} \left(r \frac{\partial \Phi}{\partial r} \right). \tag{6.14}$$

In a multicore situation, coupled differential equations for the $\Phi_n(r, t)$ of each core would result from relating E_{zR} , E_{zL} to the voltages on adjacent cores (or between the core and the conducting end plates).

Single core example: Application of the model to the case of a single core will illustrate the key features that play a role in the distribution of the stresses in the core region. The situation we consider is a one core version of the general geometry of the DARHT-II cell (see Fig. 6.1), as indicated in the sketch in Fig. 6.10.

The core is separated from end plates on the left and right sides by Δ_1 and Δ_2 , respectively. These separations are assumed to be small compared to the core radii, so we can take the axial electric field in the gaps between the conducting end plates and the core to be approximately constant. Since the electric field in the gap region is purely electrostatic (has zero curl), we can relate these axial electric fields to the voltages we defined along the core boundary as

$$\begin{aligned} E_{zL} &= -\Psi_L(r)/\Delta_1, \\ E_{zR} &= \Psi_R(r)/\Delta_2. \end{aligned} \tag{6.15}$$

Using these relations in Eq. (6.14) together with the voltage definitions in Eq. (6.12) we have the following differential equation for the “electrostatic voltage” Φ ,

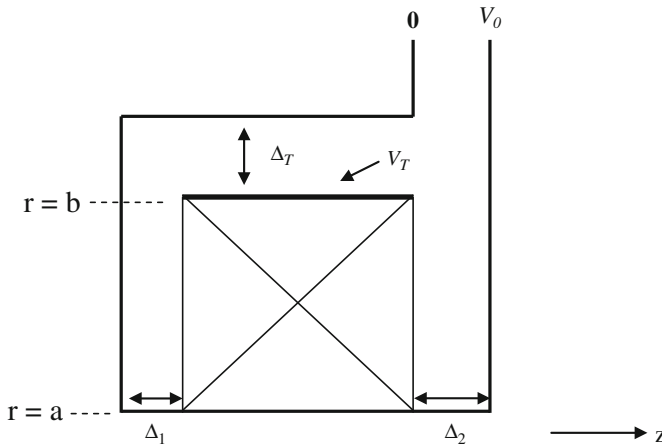


Fig. 6.10 Single core example. Note that the terminal voltage $V_0 = \Psi_L(b) - \Psi_R(b) = V(b)$ is the total inductive voltage across the core

$$\frac{1}{r} \frac{\partial}{\partial r} r \frac{\partial \Phi}{\partial r} - \kappa^2 \Phi = \kappa^2 \left(\frac{\Delta_2 - \Delta_1}{\Delta_2 + \Delta_1} \right) \frac{V(r, t)}{2} \quad (6.16)$$

Here,

$$\kappa^2 \equiv \frac{\epsilon_g}{\epsilon_r w} \left(\frac{1}{\Delta_1} + \frac{1}{\Delta_2} \right).$$

The solution of the homogeneous equation is a linear combination of modified Bessel functions, $I_0(\kappa r)$ and $K_0(\kappa r)$. The scale length of the exponential decay and growth described by these functions ($K_0(\kappa r) \sim \exp(-\kappa r)/\sqrt{\kappa r}$) can be quite short. For example, using parameters similar to those of the DARHT-II cell, $\Delta_1 = \Delta_2 = 1/4$ in., $w = 4$ in., $\epsilon_r = 12$, and $\epsilon_g = 2.3$, we have $1/\kappa \equiv \ell_c = 1.7$ in. compared to an outer radius of the core of order 30 in. With equal gap spacings the inductive voltage source term on the right hand side of Eq. (6.16) vanishes, and Φ contains only the homogeneous solution. Boundary conditions on $\Phi(r = b)$ will come from the condition of no net charge on the outer metallic band (or outermost winding) of the core. Since the inductive component of $E_r(r, z, t)$ as we have defined it in Eq. (6.9) has no average value over the core width w , no net charge requires

$$-\epsilon_r \left(\frac{\partial \Phi}{\partial r} \right)_{r=b} = \frac{\epsilon_T V_T}{\Delta_T}. \quad (6.17)$$

Here the voltage on the outer metallic band V_T is equal to $\Psi_L(r = b)$, ϵ_T is the dielectric constant of the media between the outer band and the conducting enclosure (see Fig. 6.10), and Δ_T is the separation between them (assumed to be much less than the core width w).

Assuming $\ell_c \ll b$ the approximate solution for the electrostatic voltage is

$$\Phi = \Phi(b) e^{-(b-r)/\ell_c}. \quad (6.18)$$

Using this approximation, the following expression for the voltage on the top band can be derived

$$V_T = \frac{V_0/2}{1 + \frac{\ell_c \epsilon_T}{\Delta_T \epsilon_r}}. \quad (6.19)$$

Here $V_0 = V(r = b)$ is the total voltage across the core. If the outer enclosure was a long distance from the core ($\Delta_T \rightarrow \infty$), the outer band would be at 1/2 the total voltage, and the axial electric fields on the left and right side would be equal, as might be expected with equal gap widths.

Using the above ‘‘DARHT-II like’’ parameter set with $\Delta_T = 1$ inch and $\epsilon_T = \epsilon_g = 2.3$, we find $V_T = 0.76(V_0/2)$ and a ratio of electric fields at the outer radius of $E_{zR}/E_{zL} = 1.6$. The capacitive coupling from the outer band of the core to the adjacent metallic enclosure at ground potential depresses its potential and makes for a 60% inequality in the gap stresses. As we come in from the outer radius, however, the gap stresses become equal since $\Phi(r)$ decays exponentially. This ‘‘equipartition’’ of the electrical stress in the gaps well inboard of the outer band is actually a very general property. It also applies to unequal gaps and multicore geometries when the scale length for decay of the electrostatic voltage is small compared to the scale length over which $V(r)$ varies. With unequal gaps in the single core case, for example, the approximate particular solution to the inhomogeneous Eq. (6.16) under these assumptions is

$$\Phi_P(r, t) = \frac{\Delta_1 - \Delta_2}{\Delta_1 + \Delta_2} \frac{V(r, t)}{2}. \quad (6.20)$$

At radial distances of several ℓ_c inward from the outer band, where the homogeneous contribution to Φ has decayed away, from Eq. (6.20) we find the same axial electric field in the left and right sides:

$$E_{zL} \approx E_{zR} \approx -\frac{V(r, t)}{\Delta_1 + \Delta_2}. \quad (6.21)$$

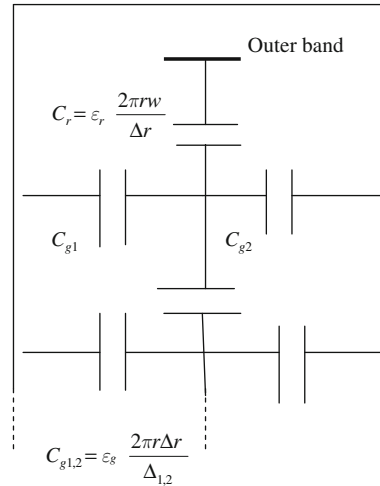
Physical interpretations: A physical interpretation of the exponentially decaying character of the homogeneous solution for $\Phi(r)$ in Eq. (6.18) can be obtained from an analysis of the distributed circuit model shown in Fig. 6.11. If we consider a layer of the core between r and $r + \delta r$, the net radial displacement current I_{disp} passing through the core at this radius r is given by

$$I_{\text{disp}} = \frac{2\pi r w \epsilon_r}{\delta r} \frac{\partial}{\partial t} [\Phi(r + \delta r) - \Phi(r)]. \quad (6.22)$$

This identifies the ‘‘core capacitance’’ of that layer $C_r = \epsilon_r 2\pi r w / \delta r$ as illustrated in Fig. 6.11.

The radial displacement current through the core decreases as we move inward since it is ‘‘shunted out’’ each side through the gap capacitances at each layer given by $C_{g1,2} = \epsilon_g 2\pi r \delta r / \Delta_{1,2}$. If we write down the differential equation for the

Fig. 6.11 Distributed circuit model of core-gap capacitive “ladder line”



electrostatic voltage $\Phi(r)$ that follows from this distributed “capacitive ladder line” model, we obtain the homogeneous version of Eq. (6.16).

Since the total electrostatic voltage drop from the outer band to ground is $\Phi(b)$, it makes sense to define an “effective core-gap capacitance” as

$$q = C_{\text{eff}}\Phi(b), \quad (6.23)$$

with q the total charge on the *inside* of the outer band. Using the approximate solution for $\Phi(r)$ in Eq. (6.18) to get the radial electric field, we have

$$C_{\text{eff}} = \epsilon_r \frac{2\pi bw}{\ell_c}. \quad (6.24)$$

Note that C_{eff} can be measured directly by applying an AC voltage between the outer band and the grounded end plates (with the outer cylinder removed). The capacitance of the outer band to the cylindrical enclosure is $C_T = \epsilon_T 2\pi bw / \Delta_T$. In the equal gap case where the band voltage is $V_T = V(b)/2 + \Phi(b)$, the condition of no net charge on the outer band leads directly to

$$V_T = \frac{V(b)/2}{1 + C_T/C_{\text{eff}}}, \quad (6.25)$$

in agreement with Eq. (6.19). This illustrates the physical point that the deviation from a simple equal division of inductive voltage across the two gaps is due to the capacitance of the outer band to the outer wall at ground potential. It also shows that it is the ratio of this capacitance to an “effective core-gap” capacitance that enters into the voltage distribution.

Generalizations: The generalization of this analytical model to multi-core situations is straightforward but tedious [17]. In that case a set of decay lengths equal to

the number of cores is obtained, but the general features of enhanced stress between the cores (and between laminations near the outer band) from capacitive coupling to the surrounding enclosure apply there also. The enhanced stress can be quite substantial as was found in the DARHT-II cell refurbishment project.

6.10 Coupling Impedance

Linear induction accelerators for electrons have almost always been designed for beam currents of a kiloAmp or more. At these currents, reduction of the transverse impedance that controls the growth rate of the “beam breakup instability” (BBU) has been a dominant concern. In linear induction accelerators for ions, or induction synchrotrons, the longitudinal impedance is generally of greater concern than the transverse impedance since the beam is not as “stiff” longitudinally. A typical induction cell can support a number of RF modes in the frequency band below the cutoff frequency for propagation in the beam pipe. These modes are confined to the vicinity of that cell, and the modes with the highest Q 's are the main contributors to the interaction impedance. The reduction of the Q 's of these modes has therefore been a major factor in the design of induction cells.

Since the vast majority of the induction cells that have been designed and constructed have been for electron linear accelerators, the reduction of the transverse impedance has been studied to a much greater extent than the longitudinal impedance. We will therefore use it as our example to illustrate the general approaches used to minimize the coupling impedances in induction cells.

6.10.1 General Form of the Transverse Impedance

We consider induction cavities of the general form shown in Figs. 6.1 and 6.2. The accelerating gap has a width w of the shortest point across the rounded electrodes, and the beam tube radius is b . The objective in this section is to derive a general form for the transverse impedance in terms of the RF magnetic fields in the gap region. In Sect. 6.10.3 we discuss how measurements of these fields can be used to deduce the transverse impedance.

To formulate an expression for the transverse impedance, consider a relativistic electron beam of current I oscillating transversely with a small amplitude Δ_x in the x direction at a frequency ω as $\exp(i\omega t)$. Inside a conducting beam tube (away from the gap region), the beam displacement induces a dipole component of the surface current on the tube wall equal to

$$K_Z = -\frac{I\Delta_x}{\pi b^2} \cos\theta = K_{z0} \cos\theta. \quad (6.26)$$

The beam also induces a dipole surface charge K_z/c on the tube wall. The collective forces from the dipole surface charge (attractive) and the dipole surface current (repulsive) cancel inside a smooth conducting tube for a highly relativistic beam, as is well known. When the beam passes through an accelerating gap region, the dipole surface current flows out into the accelerator cell, destroying this force balance. We consider here the frequency spectrum below the cutoff for propagation in the beam tube ($\omega < \omega_{co} = 1.84c/b$) where the dipole RF modes of the cell excited by the beam oscillation lead to localized deflection forces on the beam.

To describe the cell RF excitation and the fields that produce a net transverse force, the following superposition construct is useful. Place ideal surface current and surface charge sources at the radius b across the gap equal to those that would be induced in a smooth conducting tube given above. The net force from these sources and the surface current and charge on the beam tube outside the gap region will sum to zero, obviously, since the fields are the same as in a smooth tube without the gap. Then, we must add surface current and surface charge sources across the gap of the opposite sign to return to the actual situation. The fields created by these localized “negative” surface current and surface charge sources across the gap (the “cell fields”) give the net force on the beam.

To determine the net transverse impulse imparted to the electrons passing through the gap region of one cell, we need to integrate the transverse electromagnetic force $E + v \times B$ along the electron trajectory in z (assumed to be at a constant displacement from the axis through the gap region). For highly relativistic electrons, the case we consider here, it can be proven that this integral is independent of radial position anywhere inside the beam tube. Using this theorem, we can relate the change in transverse momentum to the radial magnetic field and azimuthal electric field at the gap (i.e., at the beam tube radius). With a gap width much less than the beam tube radius and the wavelength, it is physically obvious that the integral of the azimuthal electric field will be very small since it is shorted out on both sides of the gap. With this assumption, the change in transverse momentum is given by

$$\delta p_x = -e \int dz B_r(r = b, \theta = \pi/2). \quad (6.27)$$

The radial magnetic field at the gap is linearly proportional to the strength of the oscillating beam’s dipole moment, or equivalently the surface current source K_{z0} (and it varies as $\sin \theta$). The electromagnetic response of the cell itself can therefore be incorporated into a dimensionless (complex, frequency dependent) parameter defined by

$$\eta(\omega) = -\frac{1}{w} \int dz \frac{B_r(b)}{\mu_0 K_{z0}} = -\left\langle \frac{B_r(b)}{\mu_0 K_{z0}} \right\rangle. \quad (6.28)$$

Here, $B_r(b)$ is shorthand notation for the radial field at $r = b$ and $\theta = \pi/2$ in Eq. (6.27), and we use $\langle \rangle$ to imply an average in z over the gap. We introduce the definition of transverse interaction impedance Z_t through

$$\delta p_x = -i \frac{e}{c} Z_t I \Delta x. \quad (6.29)$$

Inserting this definition in Eq. (6.27), and using Eqs. (6.26) and (6.28), we obtain

$$Z_t = -i \sqrt{\frac{\mu_0}{\epsilon_0}} \frac{w}{\pi b^2} \eta \quad (6.30)$$

with η defined by Eq. (6.28).

We expect there will be one or more dipole eigenmodes of the induction cell. Calculations (or measurements) of $\eta(\omega)$ and $Z_t(\omega)$ will exhibit the usual resonance structure with a peak in the real part of $Z_t(\omega)$ at any given eigenmode frequency and a bandwidth proportional to $1/Q$.

A similar form for the peak value of the resistive part of the transverse impedance was introduced originally in computational studies of the transverse impedance in induction cells [18], as

$$Z_{tr} = \sqrt{\frac{\mu_0}{\epsilon_0}} \frac{w}{\pi b^2} \eta_f. \quad (6.31)$$

At that time η_f was considered to be a convenient figure of merit, a dimensionless “form factor” that could be reduced to of order unity in a well damped induction cell. The derivation here identifies η_f as the peak value of $\text{Im } \eta(\omega)$ as defined by Eq. (6.28), and it also provides a physical interpretation of this form factor in terms of the cell fields and equivalent source currents.

6.10.2 *Minimizing the Transverse Impedance in Induction Cell Designs*

Equation (6.30) shows that the fundamental geometrical scaling factor in the transverse impedance is w/b^2 . The peak electric field stress on the negative electrode generally constrains how small the gap width can be for a given acceleration voltage. As far as the beam pipe radius is concerned, the voltage gradient, and the cost, are adversely affected by significant increases in the inner bore as discussed in the previous subsections. So the main emphasis in the cell design has generally been placed on minimizing the Q 's to make $\eta_f = \max \text{Im } \eta(\omega)$ as small as possible, with w/b^2 determined mainly by voltage holding and economic constraints.

In contrast to RF linacs, an induction cell does not need to support a high Q acceleration mode. In ferrite induction cells, the ferrite core itself provides significant absorption of the RF modes. In addition, the placement of smaller amounts of ferrite damping material in strategic locations in the cell to further lower the Q 's of the transverse modes has now become standard practice in the design of high current electron induction accelerators. In the ATA accelerator, for example, the Q of the dominant mode at 820 MHz was reduced from 70 to 10

by adding the “mode damping ferrite” tiles on the flat-faced drive blades and back plate indicated in Fig. 6.2.

Judicious choices of ferrite tile thickness can also be used to minimize wave reflection over the most important frequency band, a well known feature of ferrite material used as UHF absorbers when they are placed against a highly conducting plate (thinner is sometimes better!). In general, the utilization and optimization of these ferrite dampers is the most powerful technique that one can use to minimize the transverse interaction impedance in induction linacs.

The other geometrical feature that can be exploited to minimize the impedance is the shape of the conductors in the vacuum region adjacent to the insulator. The importance of this geometrical feature was shown many years ago in ATA cell impedance studies [19]. In the ATA cell the insulator was located between the outer cylindrical walls just beyond the outer radius of the radial line, as shown in Fig. 6.2. The corner reflector shown in Fig. 6.2 faced the insulator at the Brewster angle (in that case) to reduce wave reflections from the vacuum-insulator interface. With this corner reflector and the ferrite dampers on the drive blades and the back wall, the Q of the dominant mode was reduced even further, to about 4.

Computational models of increasing complexity have also been developed more recently as a tool to optimize the design of induction cells for minimum transverse impedance. These computational tools were not available when the ATA, FXR, and ETA-II machines were designed and constructed, but they have proven to be a useful tool in the design of the short pulse DARHT-I cell as well as the DARHT-II cell shown in Fig. 6.1. Form factors for some of these accelerators have been calculated with these tools [18].

6.10.3 Measurement of the Transverse Impedance

The first measurements of transverse impedance were made using the same kind of techniques used to characterize RF cavities, namely excitation and detection of the modes in the cell with small RF loops placed at two different locations inside the cell. The Q of a given mode was measured by sweeping the frequency through its resonance, and the Z_{\perp}/Q was inferred from shifts of the resonant frequency induced by inserting a conducting rod (for example) along the axis of the beamtube [19]. Unfortunately, this technique cannot be used to measure the impedance of a damped cell where the Q 's are reduced to small values, because the frequency shifts are then too small compared to the bandwidth.

A technique that is more useful for the measurement of broad band impedances involves exciting fields in the cell by a twin lead placed along the axis. Beam tubes with a length several times their diameter are placed on either side of the accelerating gap to ensure that the localized cell fields (below cutoff) die out before reaching the end of the test system. The role of the twin lead is to induce a dipole surface current in the beam tubes of the same form as Eq. (6.26), except that Δ_x is now the spacing of the wires and $\pm I$ is the current in each wire. To accurately simulate the beam, the wave launched on the twin lead should be a pure forward (or backward)

traveling wave, that is, reflections from the interaction with the gap should be a small perturbation. This sets an upper bound on the spacing of the wires that can be used to measure a given cell impedance and mode Q .

The impedance of the cell at any given frequency can be deduced from the perturbation in the transmitted signal due to the cell, i.e., by measuring S_{12} with a network analyzer. For accurate results, application of this technique involves a measurement of the transmission coefficient with the cell replaced by a smooth beam tube, and then subtracting this result from a measurement of the transmission with the cell in place. This technique was used to measure the transverse impedance of DARHT-I prototype cells, for example [20]. The main limitation in this approach comes from the fact that two comparable numbers must be subtracted to deduce the impedance. As a result, the accuracy of the dimensional parameters and the two S_{12} measurements must be very good to get a meaningful result.

An alternate approach was developed in the design and prototype testing of the DARHT-II induction linac cells [21, 22]. This approach also uses a twin lead to excite the RF fields in the cell, but it relies on a measurement of the radial dipole RF magnetic field in the gap [$B_r(b)$] and the azimuthal dipole RF magnetic field in the beam tube away from the gap to determine $\eta(\omega)$ experimentally (from their ratio).

With a pure traveling wave set up by the twin lead, a measurement of the dipole B_θ at the wall some distance axially from the accelerator gap provides a direct measure of the magnitude of the “source current” in Eq. (6.26). The distance from the gap must be large enough for the cell fields (the fields created by the equivalent “negative” surface current and surface charge across the gap discussed above) to die out. The phase must be adjusted according to the distance from the loop to the gap center.

In the DARHT-II accelerator cell shown in Fig. 6.1, the loop to measure the radial RF magnetic field was inserted into the gap at a radius $r = r_p$ where the gap was a minimum (about 1.25 in. out from the beam tube radius of 5 in.). To obtain a more accurate measure of the axially-averaged radial field at $r = b$ [$\langle B_r(r = b) \rangle$] that enters into the definition of η [see Eq. (6.28)], an interpolation scheme was used [21, 22]. This interpolation related the radial field at $r = b$ to the measured radial field at $r = r_p$, using a measurement of the azimuthal field in the gap at $r = r_p$, $\theta = 0$.

$$r_p \langle B_r(r_p) \rangle - b \langle B_r(b) \rangle = \int_b^{r_p} dr \langle B_\theta(r) \rangle \approx (r_p - b) \langle B_\theta(r_p) \rangle. \quad (6.32)$$

The transverse impedance measurements of the DARHT-II cell obtained with this technique are presented in Fig. 6.12. As this data shows, the thin ferrite tiles inserted on the radial wall behind the insulator very effectively damped the modes. Using the DARHT-II cell dimensions in Eq. (6.30), the resistive impedance is $189 \text{ Im}(\eta) \Omega/\text{m}$, giving a predicted (and observed) BBU growth rate that is minimal at beam currents of 1.5–2 kA.

We should note that we made an implicit assumption in this formulation and measurement technique that the gap width is small compared to the tube radius

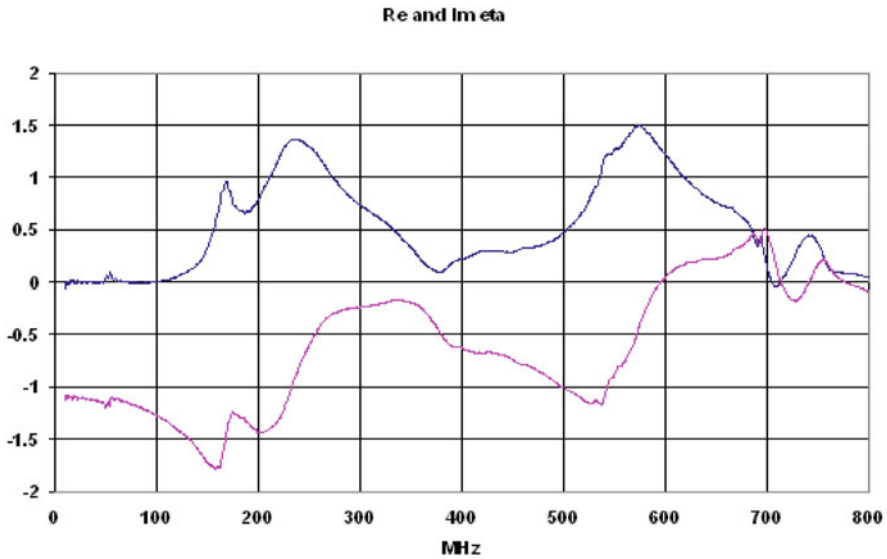


Fig. 6.12 Measurement of the real part of $\eta(\omega)$ (*lower curve*) and the imaginary part of $\eta(\omega)$ (*upper curve*) for the DARHT-II induction cell

(and wavelength). The force from the azimuthal electric field in the gap region could then be ignored compared to the radial magnetic field. Godfrey [23] has considered the contribution of the electric field to the transverse impedance for gap widths comparable or larger than the beam pipe radius. That case can lead to so-called “trapped modes” near cutoff when the gap width is larger, which can be especially dangerous because they are not damped by the cell design techniques discussed in Sect. 6.10.2.

6.11 High Average Power

Most induction accelerators constructed in the past have operated at very low average power. The heat generated by core losses was dissipated through natural conduction and convection without additional cooling. A small induction accelerator for food processing and the ETA-II were designed for high (kHz) repetition rates. Induction cell design for high repetition rates or high average power requires that an active cooling system be incorporated into the cell to insure that the average core temperature does not exceed certain limits. Short-pulse accelerators that use ferrites can be cooled by making toroids thinner, creating many cooling channels which allow circulation of the insulating fluid for heat removal. Long-pulse cells, which use tape wound cores, pose a more difficult problem. The ribbon width is limited and it must be exposed to the cooling fluid and still maintain the required voltage insulation between layers. No doubt, an induction cell for high average power poses a much greater challenge and requires careful cell design to satisfy all requirements.

Induction cells in a synchrotron to provide acceleration and longitudinal focusing must operate at high repetition rates as discussed extensively in [Chap. 11](#). This application has used Finemet and cooling studies indicate that in order to maintain safe temperature rise, a thinner material had to be used with a flux swing a small fraction of the total saturation flux swing, ΔB . Details of these developments are reported in [Chap. 11](#). A proposed accelerator for free electron lasers (FEL) operating at 5 kHz CW required 1 m diameter toroids, 8 mm thick with 2 mm cooling channels to keep the PE11B or PE11BL ferrite temperature within bounds [24].

Another issue which must be taken into consideration in the cell design is the condition created when the beam load is missing. The loss of beam current can occur when there is a failure in the injector or the magnet transport system. Since the pulse generator (modulator) is designed to operate into a matched impedance including the beam, when the beam is absent, the cell voltage will step-up by an amount which is proportional to the ratio of total current to the current without the beam load. If the beam current is a very large fraction of the total current, near voltage doubling can occur at the acceleration gap if the beam is absent. The safety factors in the core volt-seconds are typically quite small and any voltage step-up will cause core saturation and voltage reversal. Depending on the severity of the saturation, nearly 100% voltage reversal can occur which can lead to breakdowns unless proper safety factors are incorporated. To prevent voltage reversal, clamping diodes are typically installed at the modulator output.

6.12 Summary of Cell Design

The requirements of the experimental program determine the basic accelerator parameters such as energy, current, pulse duration and repetition rate. Once these parameters are established, beam transport physics determine the gradient and inside radius to insure that the design is well within the stable operating range for beam breakup instabilities. The gradient and repetition rate give guidelines to establish the basic modulator technology. For example, at very low repetition rates it is acceptable to use spark gaps as switches, at medium repetition rates, thyratrons may be more appropriate and at very high repetition rates only solid state devices will be applicable. For an optimized design, it is important to determine the technology since the operating voltage level of the modulator will strongly influence the design of the cell. If spark gaps are used, a smaller number of cells at very high voltage can meet the energy requirements. If solid state devices are used, an intermediate step-up transformer or a much larger number of cells at lower voltage will be required. The cell design and choice of magnetic material to achieve the desired voltage, current and pulse duration are always done in concert with the modulator design. Once a final design is chosen a full scale prototype must be constructed to insure that all the required parameters are met and impedance measurements are made to insure that the beam breakup growth is acceptable. Extensive prototype testing at and well above the normal operating levels must also be performed to insure that the safety factors are met for long term operation.

References

1. A. Faltens, D. Keefe, W. Salsig, and E. Hartwig. Preliminary Hardware Concepts for an Electron Ring Accelerator. *IEEE Trans. Nucl. Sci.*, NS-18:479–487, 1971. (Proceedings of the 1971 Particle Accelerator Conference, Chicago, IL, 1–3 March, IEEE).
2. L. Reginato, D. Branum, E. Cook, C. Fong, and D. Kippenhan. Advanced Test Accelerator (ATA) Pulse Power Technology Development. *IEEE Trans. Nucl. Sci.*, NS-28:2758, 1981.
3. D. Prono, D. Barret, E. Bowles, G. Caporaso, Y.-J. Chen, J. Clark, F. Coffield, M. Newton, W. Nexsen, D. Ravenscroft, W. Turner, and J. Watson. High Average Power Induction Linacs. In *Proceedings of the 1989 Particle Accelerator Conference*, page 1441, Chicago, IL, 20–23 Mar. 1989.
4. N. Christofilos, R. Hester, W. Lamb, D. Reagan, W. Sherwood, and R. Wright. High Current Linear Induction Accelerators for Electrons. *Rev. Sci. Inst.*, 35:886–890, 1964.
5. J. Beal, N. Christofilos, and R. Hester. The Astron Accelerator. *IEEE Trans. Nucl. Sci.*, NS-16:294, 1969.
6. W. Waldron and L. Reginato. Design and Performance of the DARHT Second-Axis Induction Cells and Drivers. In *Proceedings of the 24th-International Power Modulator Symposium*, pages 179–182, 26–29 June, Norfolk, VA, 2000.
7. W. Turner, G. Caporaso, G. D. Craig, J. De Ford, L. Reginato, S. Sampayan, R. Kuenning, and I. Smith. Impedance Characteristics of Induction Accelerator Cells. In *Proceedings of the 7th International Conference on High Power Particle Beams*, page 845, Karlsruhe, Germany, 4–8 July 1988.
8. J. Leiss, N. Norris, and M. Wilson. The Design and Performance of a Long Pulse High Current Linear Induction Accelerator at the National Bureau of Standards. *Part. Accel.*, 10:223–234, 1980.
9. A. Sessler and S. Yu. Relativistic Klystron Two-Beam Accelerator. *Phys. Rev. Lett.*, 54:889, 1987.
10. G. Westenskow and T. Houck. Relativistic Klystron Two-Beam Accelerator. *IEEE Trans. Plasma Sci.*, 22:750, 1994.
11. L. Reginato. Engineering Conceptual Design of the Relativistic Klystron Two-Beam Accelerator Based Power Source for 1-TeV Next Linear Collider. In *Proceedings of the 1995 Particle Accelerator Conference*, page 743, Dallas, TX, 1–5 May 1995.
12. L. Reginato. Induction Accelerator Development for Heavy Ion Fusion. *Nuovo Cimento Soc. Ital. Fis.*, 106:1445, 1993. (also Proceedings of the International Symposium on Heavy Ion Fusion, Frascati, Italy, 25–28 May, 1993).
13. T. Houck, F. Deadrick, G. Giordano, E. Henestroza, S. Lidia, L. Reginato, D. Vanecek, G. Westenskow, and S. Yu. Prototype Microwave Source for a Relativistic-Klystron Two-Beam Accelerator. *IEEE Trans. Plasma Sci.*, 24:938, 1996.
14. H. Kirk, R. Palmer, I. Gallardo, D. Kaplan, M. Green, L. Reginato, S. Yu, and Y. Fukui. Phase Rotation at the Front End of a Neutrino Factory. In *Proceedings of the 2001 Particle Accelerator Conference*, page 2026, Chicago, IL, 18–22 June 2001.
15. T. L. Houck, G. Caporaso, C. Shang, S. Sampayan, N. Molau, and M. Kro. Measured and Theoretical Characterization of the RF Properties of Stacked High-Gradient Insulator Material. In *Proceedings of the 1997 Particle Accelerator Conference*, page 2627, Vancouver, Canada, 12–16 May 1997.
16. S. E. Sampayan, G. Caporaso, D. Sanders, D. Stoddard, R. Trimble, T. Elizondo, and M. Krogh. High performance Insulator Structures for Accelerator Applications. In *Proceedings of the 1997 Particle Accelerator Conference*, page 1308, Vancouver, Canada, 12–16 May 1997.
17. R. Briggs and W. Fawley. A Simple Model for Induction Core Voltage Distributions. Technical Report LBNL-55079, Lawrence Berkeley National Laboratory, 2004. (also DARHT Tech Note No. 418).
18. C. Shang, Y.-J. Chen, T. Houck, G. Caporaso, W. Ng, N. Molau, J. Fockler, and S. Gregory. BBU Design of Linear Induction Accelerator Cells for Radiography Applications. In

- Proceedings of the 1997 Particle Accelerator Conference*, pages 2632–2635, Vancouver, Canada, 12–16 May 1997.
19. R. Briggs, D. Birx., G. Caporaso, K. Neil, and T. Genoni. Theoretical and Experimental Investigation of the Interaction Impedances and Q Values of the Accelerating Cells in the Advanced Test Accelerator. *Part. Accel.*, 18:41, 1985.
 20. L. Walling, P. Allison, M. Burns, D. Liska, D. McMurray, and A. Shapiro. Transverse Impedance Measurements of Prototype Cavities for a Dual-Axis Radiographic Hydrotest (DARHT) Facility. In *Proceedings of the 1991 Particle Accelerator Conference*, page 2961, San Francisco, CA, 6–9 May 1991.
 21. R. Briggs, D. Birx, S. Nelson, L. Reginato, and M. Vella. Transverse Impedance Measurements of the DARHT-2 Accelerator Cell. In *Proceedings of the 2001 Particle Accelerator Conference*, pages TPH079, 1850, Chicago, IL, 18–22 June 2001.
 22. R. Briggs and W. Fawley. Campaign to Minimize the Transverse Impedance of the DARHT-2 Induction Linac Cells. Technical Report LBNL-56796, Lawrence Berkeley National Laboratory, 2005. (also DARHT Tech Note No. 424).
 23. B. Godfrey, Transverse Wake Potentials for Wide Radial Lines, MRC/ABQ-R-1046, March 1988 (unpublished).
 24. J. Van Sant, Cooling Induction Accelerator Cores by Forced Flow Boiling PE11B Ferrite, Unpublished Beam Research Program Notes, Lawrence Livermore National Laboratory, 1986.